This is a repository copy of *Isogeometric analysis of fracture propagation in saturated porous media due to a pressurised non-Newtonian fluid*.

White Rose Research Online URL for this paper:
http://eprints.whiterose.ac.uk/146635/

Version: Published Version

Article:
Hageman, T., Fathima, K.M.P. and de Borst, R. orcid.org/0000-0002-3457-3574 (2019) Isogeometric analysis of fracture propagation in saturated porous media due to a pressurised non-Newtonian fluid. Computers and Geotechnics, 112. pp. 272-283. ISSN 0266-352X

https://doi.org/10.1016/j.compgeo.2019.04.030

Reuse
This article is distributed under the terms of the Creative Commons Attribution-NonCommercial-NoDerivs (CC BY-NC-ND) licence. This licence only allows you to download this work and share it with others as long as you credit the authors, but you can't change the article in any way or use it commercially. More information and the full terms of the licence here: https://creativecommons.org/licenses/

Takedown
If you consider content in White Rose Research Online to be in breach of UK law, please notify us by emailing eprints@whiterose.ac.uk including the URL of the record and the reason for the withdrawal request.

eprints@whiterose.ac.uk
https://eprints.whiterose.ac.uk/

Computers and Geotechnics 112 (2019) 272–283

Contents lists available at ScienceDirect

Computers and Geotechnics

journal homepage: www.elsevier.com/locate/compgeo

Research Paper

Isogeometric analysis of fracture propagation in saturated porous media due to a pressurised non-Newtonian fluid

Tim Hageman, K.M. Pervaiz Fathima, René de Borst*

Department of Civil and Structural Engineering, University of Sheffield, Sheffield S1 3JD, UK

ARTICLE INFO

Keywords:
Fracture
Poroelasticity
Non-Newtonian fluids
Isogeometric analysis
Interface elements

ABSTRACT

A model has been developed to simulate fractures which are pressurised using a non-Newtonian (power-law) fluid. The flow in the surrounding, deformable porous medium is described with a non-Newtonian fluid as well. The resulting model can represent the propagation of pressurised fractures, leak-off and the interstitial fluid pressure in a saturated porous medium. The resulting equations have been discretised using Non-Uniform Rational B-Splines (NURBS), cast into a traditional finite element datastructure using Bézier extraction. It is shown that lumped integration of the fracture inflow terms is needed to obtain non-oscillatory results for the fluid velocity normal to the discontinuity, and an integration scheme has been derived to prevent non-physical fluid leak-off from the fracture tips. Simulations have been carried out for a typical hydraulic fracture problem. The results show the dependence of the fluid leak-off and the fracture tip pressure on the power-law fluid index. Shear-thinning fluids result in a larger amount of fluid leak-off compared to Newtonian fluids, but their lower effective viscosity results in a higher pressure at the fracture tip. These effects influence the propagation velocity of the pressurised fracture, and thus demonstrate the importance of properly modelling the non-Newtonian character of pressurising fluids.

1. Introduction

Fracture in porous materials saturated with non-Newtonian fluids occurs in many applications including hydraulic fracturing, contaminant transport, geothermal energy storage, biological tissues etc. Modelling fluid-driven fractures is a challenging problem because of the strong coupling between the mechanical deformation and the fluid pressure, which results in a strongly nonlinear response. Fluid flow inside fractures and the exchange between the fluid in the fracture and the interstitial fluid in the surrounding porous medium further increase the coupling and nonlinearity. An additional challenge is the fact that in many applications the fluid is non-Newtonian, resulting in fluid velocities being non-linearly dependent on the pressure gradients.

One of the first simulations in which fluid-driven fracture propagation was modelled successfully combined finite elements for the poroelastic medium with a finite difference method to capture the fluid flow inside the fracture [1]. Later, more advanced discretisation techniques were proposed to model fracture propagation in saturated porous media. Hydromechanical interface elements, which are relatively simple to implement, were introduced within the setting of a standard finite element approach [2]. This approach can be very effective when the crack path is known beforehand. For freely propagating cracks, remeshing [3,4] or the extended finite element method (XFEM) are appropriate solutions [5–9] to overcome this limitation by decoupling the crack path from the original mesh. Recently, phase-field methods have also successfully incorporated fluid transport inside fractures, paving the way for smeared approaches [10].

Recent advances allow Non-Uniform Rational B-Splines (NURBS) to use standard finite element data structures through Bézier extraction [11]. The use of NURBS has the advantage of higher-order continuity and therefore more accurately captures stress and pressure gradients at the fracture tip. The formulation using NURBS was extended to interface elements, but a lumped integration scheme appeared necessary to prevent traction oscillations [12]. NURBS were used to model fracturing poroelastic media [13], and were used also to simulate fluid transport inside fractures using a subgrid scale model [14].

Pressurised fractures have been simulated assuming a continuous pressure across the fracture [15]. Assuming a continuous pressure inside the fracture necessarily leads to a small boundary layer within the porous medium at the crack face with a reduced permeability. Indeed, numerical solutions use very dense meshes [15]. Another solution is to consider a discontinuous pressure model with independent pressure degrees of freedom on each of the crack faces and for the fluid within the fracture [8,16,17]. This three degree of freedom pressure model is

* Corresponding author.
E-mail address: r.deborst@sheffield.ac.uk (R. de Borst).

https://doi.org/10.1016/j.compgeo.2019.04.030
Received 18 February 2019; Received in revised form 1 April 2019; Accepted 27 April 2019
0266-352X/ © 2019 The Author(s). Published by Elsevier Ltd. This is an open access article under the CC BY-NC-ND license (http://creativecommons.org/licenses/BY-NC-ND/4.0/).

capable of successfully simulating the propagation of fluid-pressurised fractures [18,19].

The above-mentioned results are for modelling fracture propagation in porous media saturated with Newtonian fluids. For flow of non-Newtonian fluids in porous media, however, numerical simulations are very rare. Simulations which include a rigid, non-deformable porous material have been described without fractures [20,21], and with fractures [22]. Non-Newtonian (power-law) flow inside rough-walled fractures has been simulated using a finite volume method [23], and show that shear-thinning power law fluids flow faster through the fractures compared to Newtonian fluids, but that shear-thickening fluids flow considerably slower. Furthermore, it has been shown that the power-law index in power-law fluids has large effects on the flow direction inside fractures [24]. Semi-analytical solutions for time-dependent inflows showed similar trends, with shear-thinning fluids flowing faster than Newtonian fluids [25,26].

Previously, a model has been proposed which can capture flow of non-Newtonian fluids in deformable, poroelastic media in the presence of cracks [27]. Therein, the pressure across the fracture was assumed to be continuous, thus effectively precluding the modelling of fluid-pressurised fracture propagation. We now propose a formulation for fracture propagation in a saturated poroelastic medium induced by a pressurised non-Newtonian fluid. In line with the discussion before, we use an independent pressure degree of freedom to model the fluid pressure inside the discontinuity. We show that a lumped integration scheme is beneficial in removing spurious velocity oscillations at the fracture tip. Furthermore, an integration scheme is described which prevents the independent fluid pressure inside the fracture from being coupled to the independent fluid pressure inside hydromechanical interface elements where fracture has not yet started. This avoids non-physical fluid leak-off.

In the remainder of this paper, we first briefly summarise the governing equations for non-Newtonian fluid flow in a deformable, porous medium, and a model is derived to simulate fractures pressurised with a non-Newtonian power-law fluid (Section 2). These models are discretised using NURBS shape functions and cast in standard finite element format using Bézier extraction (Section 3). The discontinuity is represented by a hydromechanical interface element. Attention is given to the integration of the interface elements, resulting in a scheme which prevents pressure oscillations in the inflow. In Section 4, an example shows the effect of this integration scheme. Finally, Section 5 presents a simulation of a typical hydraulic fracturing problem to demonstrate the effect of non-Newtonian fluids.

2. Governing equations

We consider a domain Ω which consists of a porous material and is split into two parts, Ω^- and Ω^+, by a discontinuity Γ_d, see Fig. 1. To represent a fracture, Γ_d must be C^{-1} discontinuous in the displacements. For the pressure of the interstitial fluid, several models exist [16,17]. To enable pressurising a crack, there must be a difference between the fluid pressure in the crack and that in the surrounding porous medium, necessitating a jump in the pressure between the fluid in the fracture and the fluid pressure in the surrounding porous medium. This means that at each crack face we have a C^{-1} discontinuity in the fluid pressure [8], and a separate permeability can be assigned to each crack face.

2.1. Bulk

2.1.1. Deformations of the porous solid

In most poroelastic systems, the deformations of the solid occur fast compared to the pressure changes of the interstitial fluid. Therefore, the deformations can be considered the result of a quasi-static process. This assumption allows the solid deformations to be governed by the hydrostatic momentum balance:

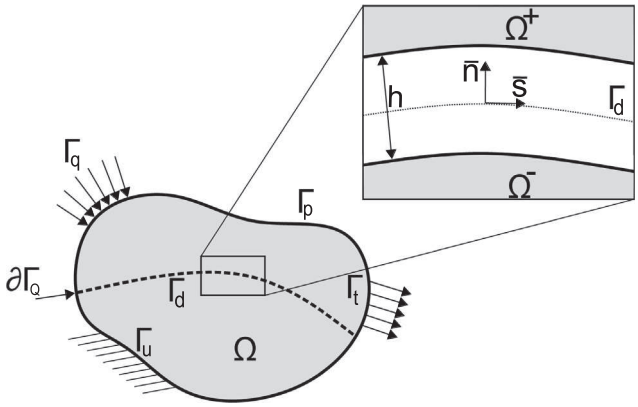

Fig. 1. Overview of the domains Ω^+ and Ω^- with the discontinuity Γ_d. The local $\bar{s}$, $\bar{n}$ coordinate system and fracture opening height h used for the analysis of the fracture are also shown.

$$\nabla\cdot\boldsymbol{\sigma} = 0 \qquad \boldsymbol{x}\in\Omega \tag{1}$$

subject to the external and internal boundary conditions:

$$\boldsymbol{u} = \bar{\boldsymbol{u}} \qquad \boldsymbol{x}\in\Gamma_u \tag{2a}$$

$$\boldsymbol{n}\cdot\boldsymbol{\sigma} = \bar{\boldsymbol{t}} \qquad \boldsymbol{x}\in\Gamma_t \tag{2b}$$

$$\boldsymbol{n}_d\cdot\boldsymbol{\sigma} = \boldsymbol{t}_{\Gamma_d} \qquad \boldsymbol{x}\in\Gamma_d \tag{2c}$$

with $\boldsymbol{u}$ the displacement of the porous material, $\bar{\boldsymbol{u}}$ the displacement prescribed at Γ_u, and $\bar{\boldsymbol{t}}$ and $\boldsymbol{t}_{\Gamma_d}$ the traction at Γ_t and Γ_d, respectively.

The total stress $\boldsymbol{\sigma}$ in a saturated porous medium is defined as:

$$\boldsymbol{\sigma} = \boldsymbol{\sigma}_s - \alpha p\boldsymbol{I} \tag{3}$$

with α the Biot coefficient, p the pressure of the interstitial fluid and $\boldsymbol{I}$ the second-order unit tensor. It is assumed that the stress inside the solid material $\boldsymbol{\sigma}_s$ is linearly related to the strain by:

$$\boldsymbol{\sigma}_s = \boldsymbol{D}:\boldsymbol{\varepsilon} \tag{4}$$

with $\boldsymbol{D}$ the fourth-order elastic stiffness tensor. The infinitesimal strain ε is obtained from $\boldsymbol{\varepsilon} = \nabla^s\boldsymbol{u}$, using the symmetrised gradient operator ∇^s.

2.1.2. Interstitial fluid pressure

The pressure in the interstitial fluid can be computed from the mass balance of the mixture, which is obtained by adding the equations for mass conservation of the fluid and solid phases:

$$\frac{1}{M}\frac{\partial p}{\partial t} + \alpha\nabla\cdot\dot{\boldsymbol{u}} + \nabla\cdot\boldsymbol{q} = 0 \qquad \boldsymbol{x}\in\Omega \tag{5}$$

with the appropriate internal and external boundary conditions:

$$p = \bar{p} \qquad \boldsymbol{x}\in\Gamma_p \tag{6a}$$

$$\boldsymbol{n}\cdot\boldsymbol{q} = \bar{q} \qquad \boldsymbol{x}\in\Gamma_q \tag{6b}$$

$$\boldsymbol{n}_d\cdot\boldsymbol{q} = \boldsymbol{n}_d\cdot\boldsymbol{q}_d \qquad \boldsymbol{x}\in\Gamma_d \tag{6c}$$

where $\bar{p}$ is the prescribed pressure at Γ_p, $\bar{q}$ is the prescribed fluid inflow in the direction of surface normal $\boldsymbol{n}$, $\boldsymbol{n}_d\cdot\boldsymbol{q}_d$ is the inflow resulting from the fracture, and M is the Biot modulus. The fluid flux $\boldsymbol{q}$ is defined as $\boldsymbol{q} = n_f(\boldsymbol{v} - \dot{\boldsymbol{u}})$, with n_f the porosity of the medium, and $\boldsymbol{v}$ and $\dot{\boldsymbol{u}}$ the velocity of the fluid and solid respectively.

The power-law model is used widely for non-Newtonian fluids. It relates the shear stress τ to the shear rate $\frac{\partial v}{\partial y}$ by:

$$\tau = \mu_0\left(\frac{\partial v}{\partial y}\right)^n \tag{7}$$

with v the fluid velocity, μ_0 the base viscosity or the consistency factor, and n the power-law fluid index. An index $n < 1$ represents shear-thinning fluids, for $n = 1$ a Newtonian fluid is obtained, and $n > 1$

represents shear-thickening fluids. This fluid model can be used inside porous media for fluids with $n < 2$, via a generalised Darcy relation:

$$\boldsymbol{q} = -k_f^* \, |\nabla p|^{\frac{1}{n}-1} \nabla p \tag{8}$$

with the effective permeability k_f^* a constant defined as [28,29]:

$$k_f^* = \frac{n}{3n+1}\left(\frac{50}{3}k\right)^{\frac{1+n}{2n}} (2C\mu_0)^{-\frac{1}{n}} n_f^{\frac{n-1}{2n}} \tag{9}$$

with k the intrinsic permeability of the porous medium and C is a constant, normally taken as $\frac{50}{24}$ [29].

2.2. Fractures

2.2.1. Interface traction

The total traction for a fully saturated fracture at Γ_d is given by:

$$\boldsymbol{t}_{\Gamma_d} = \boldsymbol{t}_d - p\boldsymbol{n}_d \tag{10}$$

The traction which stems from the fracture opening, $\boldsymbol{t}_d$, is modelled using a cohesive zone model. In a local coordinate system, the cohesive tractions $\boldsymbol{t}_d^{\text{loc}}$ are related to the jump in displacement $[\![\boldsymbol{u}]\!]$ through a non-linear relation:

$$\boldsymbol{t}_d^{\text{loc}} = \boldsymbol{t}_d^{\text{loc}}([\![\boldsymbol{u}]\!], \kappa) \tag{11}$$

where κ is a history parameter. The traction vector $\boldsymbol{t}_d^{\text{loc}}$ can be related to the tractions in the global coordinate system using the rotation matrix $\boldsymbol{R} = (\bar{\boldsymbol{s}}, \bar{\boldsymbol{n}})$ in a two dimensional configuration (Fig. 1):

$$\boldsymbol{t}_d^{\text{loc}} = \boldsymbol{R}\boldsymbol{t}_d \tag{12}$$

In this paper, an exponential traction-separation law is used, defining the traction in the normal direction as:

$$t_n = f_t \exp\left(-\frac{f_t}{G_{Ic}}[\![u]\!]_n\right) \tag{13}$$

with f_t the tensile strength of the material and G_{Ic} the mode-I fracture toughness. The traction in the tangential direction is assumed to be zero.

For use in a Newton-Raphson iterative procedure, the constitutive relation can be linearised as:

$$\mathrm{d}\boldsymbol{t}_d^{\text{loc}} = \boldsymbol{D}_d \mathrm{d}[\![\boldsymbol{u}]\!] \tag{14}$$

with d denoting a small increment and

$$\boldsymbol{D}_d = \frac{\partial \boldsymbol{t}_d^{\text{loc}}}{\partial [\![\boldsymbol{u}]\!]} \tag{15}$$

The limiting case $\boldsymbol{t}_d^{\text{loc}} = \boldsymbol{0}$ represents a traction-free crack.

In the case study, interface elements were inserted for fractured and non-fractured parts. To prevent the part of the interface which has not yet fractured from opening, a finite stiffness is assigned to these interface elements prior to crack initiation:

$$\boldsymbol{D}_d = \begin{bmatrix} d_n & 0 \\ 0 & d_s \end{bmatrix} \tag{16}$$

where d_n and d_s are dummy stiffness values in the normal and tangential directions, respectively. These values must be chosen sufficiently high to prevent any additional deformations due to the presence of the interface elements in the pre-cracking phase.

2.2.2. Fluid pressure

The fluid inside the fracture adapts fast to changes in the pressure compared to the interstitial fluid in the surrounding porous medium. Therefore, inertial effects are neglected in the formulation for the fluid in the fracture. It is furthermore assumed that the compressibility of the fluid within the fracture is small, and that effects of density gradients are negligible. The pressure inside the fracture is therefore obtained from the mass balance of an incompressible fluid:

$$\frac{\partial w}{\partial \bar{n}} + \frac{\partial v}{\partial \bar{s}} = 0 \tag{17}$$

with w the fluid velocity in fracture normal direction, and v the velocity in the tangential direction of the fracture. Integrating Eq. (17) over the fracture height results in:

$$w^+ - w^- = -\int_{-h/2}^{h/2} \frac{\partial v}{\partial \bar{s}} \, \mathrm{d}\bar{n} \tag{18}$$

with w^+ and w^- the fluid velocity at the top and bottom of the fracture. These velocities are determined using an interface permeability:

$$w^+ = k_i(p_d - p^+) + \frac{1}{2}\frac{\partial h}{\partial t} \tag{19a}$$

$$w^- = k_i(p^- - p_d) - \frac{1}{2}\frac{\partial h}{\partial t} \tag{19b}$$

and the corresponding terms for the boundary conditions in Eq. (6c) by:

$$-\boldsymbol{n}_d \cdot \boldsymbol{q}_d = k_i(p_d - p^+) \tag{20a}$$

$$\boldsymbol{n}_d \cdot \boldsymbol{q}_d = k_i(p^- - p_d) \tag{20b}$$

with k_i the interface permeability, p_d the pressure inside the discontinuity, and p^- and p^+ the interstitial fluid pressures at the interfaces inside the porous medium. While time-dependent relations for the interface permeability exist [8], a constant value for this permeability has been taken here to focus on the effect of the non-Newtonian fluid index n.

It is assumed that the tangential fluid velocity inside the fracture is high compared to the velocity normal to the fracture. Since the height of the fracture is small compared to its length, it is furthermore assumed that the pressure inside the fracture is constant in the normal direction. Using these assumptions, the balance of momentum in the tangential direction becomes:

$$0 = -\frac{\partial p_d}{\partial \bar{s}} + \frac{\partial \tau}{\partial \bar{n}} \tag{21}$$

and after substitution of the constitutive relation for the power-law fluid, Eq. (7), we obtain:

$$0 = -\frac{\partial p_d}{\partial \bar{s}} + \frac{\partial}{\partial \bar{n}}\left(\mu_0 \left(\frac{\partial v}{\partial \bar{n}}\right)^n\right) \tag{22}$$

Solving this equation with no-slip boundary conditions at $\bar{n} = \pm h/2$ results in an expression for the fluid velocity inside the fracture:

$$v(\bar{n}) = \frac{n}{n+1}\mu_0^{-\frac{1}{n}} \left|\frac{\partial p_d}{\partial \bar{s}}\right|^{\frac{1}{n}-1} \frac{\partial p_d}{\partial \bar{s}} \left(|\bar{n}|^{\frac{1}{n}+1} - \left(\frac{h}{2}\right)^{\frac{1}{n}+1}\right) \tag{23}$$

Substituting this expression for the tangential fluid velocity and that for the inflow velocity, Eq. (19), into Eq. (18) results in the following equation for the pressure p_d in the fracture:

$$k_i(2p_d - p^+ - p^-) + \frac{\partial h}{\partial t} = \frac{\partial}{\partial \bar{s}}\left(\frac{-2n}{2n+1}\mu_0^{-\frac{1}{n}} \left|\frac{\partial p_d}{\partial \bar{s}}\right|^{\frac{1}{n}-1} \frac{\partial p_d}{\partial \bar{s}} \left(\frac{h}{2}\right)^{\frac{1}{n}+2}\right) \quad \boldsymbol{x} \in \Gamma_d \tag{24}$$

with the boundary conditions

$$q_d = Q_{tip} \qquad \boldsymbol{x} \in \partial\Gamma_Q \tag{25a}$$

$$p_d = \overline{p}_d \qquad \boldsymbol{x} \in \partial\Gamma_{p_d} \tag{25b}$$

Q_{tip} being the inflow imposed on the points $\partial\Gamma_d$, and $\overline{p}_d$ being the pressure imposed on $\partial\Gamma_{p_d}$.

3. Discretisation

The weak form of the momentum balance, Eq. (1), is obtained through multiplication by the test function η and using the divergence theorem:

$$\int_\Omega \nabla\eta\colon\left(\boldsymbol{\sigma}_s - \alpha p\boldsymbol{I}\right)\mathrm{d}\Omega - \int_{\Gamma_d}\eta\cdot(\boldsymbol{t}_d - p_d\boldsymbol{n}_d)\mathrm{d}\Gamma = \int_{\Gamma_t}\eta\cdot\bar{\boldsymbol{t}}\ \mathrm{d}\Gamma \tag{26}$$

The weak form of the mass balance of the mixture, Eq. (5), is obtained through multiplication by the test function for the interstitial pressure, ζ. Using the divergence theorem and substituting the boundary conditions at the discontinuity, Eq. (20), results in:

$$\int_\Omega \alpha\zeta\nabla\cdot\dot{\boldsymbol{u}}\ \mathrm{d}\Omega + \int_\Omega k_f^*\,|\nabla p|^{1/n-1}\nabla\zeta\cdot\nabla p\ \mathrm{d}\Omega + \int_\Omega\frac{1}{M}\zeta\dot{p}\ \mathrm{d}\Omega + \int_{\Gamma_d}\zeta k_i(p-p_d)\,\mathrm{d}\Gamma = -\int_{\Gamma_q}\zeta\bar{q}\ \mathrm{d}\Gamma \tag{27}$$

Finally, the expression for the fluid pressure in the crack, p_d, is obtained by multiplying Eq. (24) by a test function for the discontinuous pressure, ξ, and again using the divergence theorem:

$$\int_{\Gamma_d} k_i\xi(p^+ + p^- - 2p_d) - \xi\frac{\partial h}{\partial t}\,\mathrm{d}\Gamma_d + \int_{\Gamma_d} -\frac{2n}{2n+1}\mu_0^{-\frac{1}{n}}\frac{\partial\xi}{\partial\bar{s}}\left|\frac{\partial p_d}{\partial\bar{s}}\right|^{\frac{1}{n}-1}\left(\frac{\partial p_d}{\partial\bar{s}}\right)\left(\frac{h}{2}\right)^{\frac{1}{n}+2}\mathrm{d}\Gamma_d = \int_{\partial\Gamma_d}\xi Q_d\mathrm{d}\partial\Gamma_d \tag{28}$$

Eqs. (26)–(28) have been discretised using Non-Uniform Rational B-Splines (NURBS), which are commonly used in IsoGeometric Analysis (IGA). In order to use NURBS in the same manner as the shape functions in standard finite element analysis, Bézier extraction has been used [11]. This allows for the deformations and pressures to be determined on a per element basis, while preserving the inter-element continuity. Using the Bézier extracted shape functions for the solid displacement $\boldsymbol{N}_s$, the interstitial fluid pressure $\boldsymbol{N}_f$, and the pressure inside the discontinuity $\boldsymbol{N}_d$, the displacements and pressures are discretised as:

$$\boldsymbol{u} = \sum_{e=1}^{n_{el}}\boldsymbol{N}_s^{el}\boldsymbol{u}^{el} \tag{29}$$

$$p = \sum_{e=1}^{n_{el}}\boldsymbol{N}_f^{el}\boldsymbol{p}^{el} \tag{30}$$

$$p_d = \sum_{e=1}^{n_{el}}\boldsymbol{N}_d^{el}\boldsymbol{p}_d^{el} \tag{31}$$

Whereas standard Lagrangian shape functions always have a C^0 inter-element continuity, NURBS of order p have a continuity of C^{p-1} between elements. This allows for continuous solutions for the stresses and fluid velocities. Since Eq. (24) contains second derivatives of the pressure, cubic NURBS were used for the interstitial and fracture pressures ($\boldsymbol{N}_f$ and $\boldsymbol{N}_d$). To prevent spurious pressure oscillations, the inf-sup condition has to be fulfilled [30]. This requirement can be met using p-refinement [14], resulting in quartic shape functions for the solid displacement ($\boldsymbol{N}_s$).

It is noted that the pressure and displacements are C^{-1} discontinuous at the interface. Furthermore, degrees of freedom for p_d are inserted in both the fractured and non-fractured interface elements, as can be seen in Fig. 2. To couple this pressure to the pressures inside the surrounding porous medium, a dummy permeability $k_{i,d}$ has been used for non-fractured elements, in a similar manner as a dummy stiffness is used for the displacements in interface elements. This dummy permeability has been combined with Eq. (20) to allow for fluid flow between Ω^+ and Ω^-.

Using the shape functions of Eqs. (29)–(31) to discretise the weak form of Eq. (26) results in:

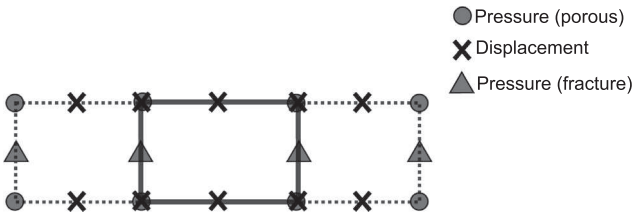

Fig. 2. Overview of the locations of the degrees of freedom for the interface elements. The pressures and displacement degrees of freedom are shown for the centre element. The vertical distance between the top and bottom has been added for visual purposes, since in reality the top and bottom of the interface coincide.

$$\boldsymbol{f}_{ext} - \boldsymbol{f}_{int} - \boldsymbol{f}_d = \boldsymbol{0} \tag{32}$$

with the external force $\boldsymbol{f}_{ext}$ defined in a standard manner as:

$$\boldsymbol{f}_{ext} = \int_{\Gamma_t}\boldsymbol{N}_s^T\bar{\boldsymbol{t}}\ \mathrm{d}\Gamma \tag{33}$$

The force resulting from the interior of Ω^+ and Ω^-, $\boldsymbol{f}_{int}$, is given by:

$$\boldsymbol{f}_{int} = \int_\Omega\boldsymbol{B}^T\boldsymbol{\sigma}_s\ \mathrm{d}\Omega - \int_\Omega\alpha\boldsymbol{B}^T\boldsymbol{m}\boldsymbol{N}_f\boldsymbol{p}^{el}\ \mathrm{d}\Omega \tag{34}$$

with $\boldsymbol{m} = [1\ 1\ 0]^T$ and $\boldsymbol{B}$ the strain-nodal displacement operator, used to map the element displacements to the strains:

$$\boldsymbol{\varepsilon} = \boldsymbol{B}\boldsymbol{u}^{el} \tag{35}$$

For the forces at the interface, it is convenient to introduce a matrix that maps the displacements to the jumps in displacement across the interface:

$$[\![\boldsymbol{u}]\!]^{el} = \boldsymbol{N}_{ds}\boldsymbol{u}^{el} \tag{36}$$

This mapping matrix is used to define the forces acting at the discontinuity, $\boldsymbol{f}_d$ as:

$$\boldsymbol{f}_d = \int_{\Gamma_d}\boldsymbol{N}_{ds}^T\boldsymbol{R}^T\boldsymbol{D}_d\boldsymbol{R}\boldsymbol{N}_{ds}\boldsymbol{u}^{el}\ \mathrm{d}\Gamma - \int_{\Gamma_d}\boldsymbol{N}_{ds}^T\boldsymbol{n}_{\Gamma_d}\boldsymbol{N}_d\boldsymbol{p}_d^{el}\ \mathrm{d}\Gamma \tag{37}$$

The mass conservation for the bulk and fracture contains time derivatives, which are discretised using a backward finite difference scheme. Hence, the terms of Eq. (32) are computed at time $t + \Delta t$, and the time derivatives in the mass conservation equations are discretised as:

$$\dot{\square} = \frac{\square^{t+\Delta t} - \square^t}{\Delta t} \tag{38}$$

The weak form of the mass conservation, Eq. (27), is discretised using the shape functions of Eqs. (29)–(31) and the time discretisation given in Eq. (38) as:

$$\boldsymbol{q}_{ext} - \boldsymbol{q}_{int} - \boldsymbol{q}_d = \boldsymbol{0} \tag{39}$$

with the external flux $\boldsymbol{q}_{ext}$ defined as:

$$\boldsymbol{q}_{ext} = \Delta t\int_{\Gamma_q}\boldsymbol{N}_f^T\bar{q}\ \mathrm{d}\Gamma \tag{40}$$

and the internal flux $\boldsymbol{q}_{int}$ as:

$$\boldsymbol{q}_{int} = -\int_\Omega\alpha\boldsymbol{N}_f^T\boldsymbol{m}^T\boldsymbol{B}(\boldsymbol{u}^{t+\Delta t} - \boldsymbol{u}^t)\,\mathrm{d}\Omega - \int_\Omega\Delta t k_f^*\,|\nabla\boldsymbol{N}_f\boldsymbol{p}^{t+\Delta t}|^{\frac{1}{n}-1}(\nabla\boldsymbol{N}_f)^T\nabla\boldsymbol{N}_f\boldsymbol{p}^{t+\Delta t}\ \mathrm{d}\Omega - \int_\Omega\frac{1}{M}\boldsymbol{N}_f^T\boldsymbol{N}_f(\boldsymbol{p}^{t+\Delta t} - \boldsymbol{p}^t)\,\mathrm{d}\Omega \tag{41}$$

The fluid fluxes due to the fracture are given by:

$$\boldsymbol{q}_d = \int_{\Gamma_d^\pm}k_i^{el}\Delta t\ \boldsymbol{N}_f^T(\boldsymbol{N}_d\boldsymbol{p}_d^{t+\Delta t} - \boldsymbol{N}_f\boldsymbol{p}^{t+\Delta t})\mathrm{d}\Gamma \tag{42}$$

with $\int_{\Gamma_d^\pm}$ indicating that the integral is performed twice, separately for the pressures at the top and at the bottom. The interface permeability of the element k_i^{el} is given by:

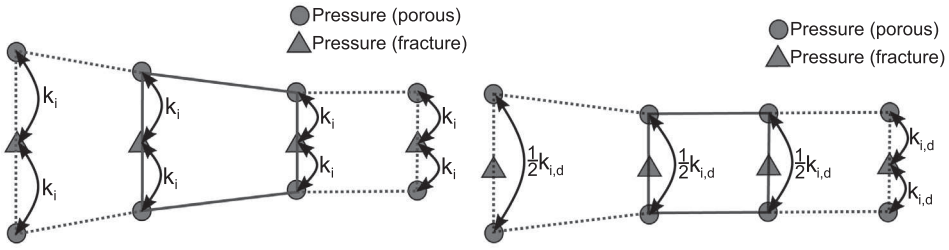

(a) Fractured element (b) Non-fractured element

Fig. 3. Schematic overview of the control-point sets integrated with lumped integration, and the corresponding k_i^{el} used per control-point set.

$$k_i^{el} = \begin{cases} k_{i,d} & \text{for non-fractured elements} \\ k_i & \text{for fractured elements} \end{cases} \tag{43}$$

The weak form for the fluid pressure inside the fracture, Eq. (28), is discretised as:

$$\boldsymbol{q}_{d,ext} - \boldsymbol{q}_{d,int} - \boldsymbol{q}_{d,d} = \boldsymbol{0} \tag{44}$$

with the external flux defined as:

$$\boldsymbol{q}_{d,ext} = \Delta t \int_{\partial\Gamma_Q} \boldsymbol{N}_d^T Q_{tip} \, \mathrm{d}\partial\Gamma \tag{45}$$

The internal flux of the fracture reads:

$$\boldsymbol{q}_{d,int} = -\Delta t \int_{\Gamma_d} \frac{2n}{2n+1} \mu_0^{-\frac{1}{n}} (\nabla \boldsymbol{N}_d)^T |\nabla \boldsymbol{N}_d \boldsymbol{p}_d^{t+\Delta t}|^{\frac{1}{n}-1} \left(\frac{\boldsymbol{n}_{\Gamma_d} \boldsymbol{N}_{ds} \boldsymbol{u}^{t+\Delta t}}{2} \right)^{\frac{1}{n}+2} \nabla \boldsymbol{N}_d \, \boldsymbol{p}_d^{t+\Delta t} \, \mathrm{d}\Gamma \tag{46}$$

and the fluxes due to the coupling between the bulk and fracture are given by:

$$\boldsymbol{q}_{d,d} = \Delta t \int_{\Gamma_d} k_i^{el} \boldsymbol{N}_d^T (\boldsymbol{N}_f \boldsymbol{p}^{+\,t+\Delta t} + \boldsymbol{N}_f \boldsymbol{p}^{-\,t+\Delta t} - 2\boldsymbol{N}_d \boldsymbol{p}_d^{t+\Delta t}) \mathrm{d}\Gamma - \int_{\Gamma_d} \boldsymbol{N}_d^T \boldsymbol{n}_{\Gamma_d}^T \boldsymbol{N}_{ds} (\boldsymbol{u}^{t+\Delta t} - \boldsymbol{u}^t) \mathrm{d}\Gamma \tag{47}$$

While most terms in Eqs. (32), (39) and (44) can be integrated with a Gauss integration scheme, this will result in traction oscillations for the interface stiffness term of Eq. (37) for non-fractured elements [13,31]. These oscillations can be prevented by using lumped integration [12], in which the internal force due to the tractions at the interface is determined per set of co-located control points instead of per element:

$$\boldsymbol{f}_d^{non-frac} = \int_{\Gamma_d} \boldsymbol{N}_{ds}^T \boldsymbol{R}^T \boldsymbol{D}_d \boldsymbol{R} \boldsymbol{N}_{ds} \boldsymbol{u}^{el} \, \mathrm{d}\Gamma = \sum_{cp=1}^{n_{cp}} \boldsymbol{M}_l^T \boldsymbol{R}^T \boldsymbol{D}_d \boldsymbol{R} \boldsymbol{M}_l \boldsymbol{u}^{cp} A_{cp} \tag{48}$$

with n_{cp} the number of control-point sets for the interface element, and $\boldsymbol{u}^{cp}$ the displacements of the control-point set. The lumped integration matrix $\boldsymbol{M}_l$ is defined by:

$$\left[\!\left[\boldsymbol{u} \right]\!\right]_{cp} = \begin{bmatrix} -1 & 1 & 0 & 0 \\ 0 & 0 & -1 & 1 \end{bmatrix} \begin{bmatrix} u_x^- \\ u_x^+ \\ u_y^- \\ u_y^+ \end{bmatrix} = \boldsymbol{M}_l \boldsymbol{u}_{cp} \tag{49}$$

and the weighting factor A_{cp} corresponding to the control-point set is given by:

$$A_{cp} = \int_{\Gamma_d} \boldsymbol{N}_s \, \mathrm{d}\Gamma \tag{50}$$

It is emphasised that lumped integration is only carried out for non-fractured elements.

It was observed that oscillations also occurred in the fracture inflow velocity, w^+ and w^-. These oscillations are caused by the coupling between the fracture pressure p_d and interstitial fluid pressure in the bulk material, Eqs. (42) and (47). To prevent these oscillations, Eq. (42) and the first term of Eq. (47) have also been integrated using lumped integration. Since the interface permeability k_i can be of the same order of magnitude as the dummy permeability $k_{i,d}$ for near-continuous pressures at the interface, lumped integration was now used for the fractured as well as for the non-fractured interface elements.

The pressure inside the discontinuity, p_d, is coupled to the interstitial pressure by k_i for fractured elements, and by $k_{i,d}$ for non-fractured elements. This coupling leads to problems around the fracture tips, where pressure degrees of freedom receive fluid due to the flow inside the fracture, and would be linked to the interstitial fluid by the dummy permeability. It would result in large amounts of outflow at the fracture tips, due to the fluid flow normal to the fracture being influenced by the large dummy permeability forcing equal pressures. To prevent these non-physical outflows, the non-fractured elements around the fracture tips have been integrated with a modified lumped integration scheme. Instead of forcing p^+ to be equal to p_d, and p_d to be equal to p^-, p^+ and p^- are directly linked, as shown in Fig. 3. This is done by replacing Eq. (42) by:

$$\boldsymbol{q}_d = \mp \int_{\Gamma_d^{\pm}} \frac{1}{2} k_{i,d} \Delta t \boldsymbol{N}_f^T (\boldsymbol{N}_f \boldsymbol{p}^+ - \boldsymbol{N}_f \boldsymbol{p}^-) \, \mathrm{d}\Gamma \tag{51}$$

This allows the continuous pressure to be enforced across the discontinuity without influencing the pressure inside the discontinuity. The effect of using this fracture tip integration will be shown in Section 4.

A Newton-Raphson iterative scheme has been used to solve Eqs. (32), (39) and (44) in a fully coupled manner, resulting in:

$$\begin{bmatrix} \boldsymbol{K} + \boldsymbol{K}_d & \boldsymbol{Q} & \boldsymbol{Q}_d \\ \boldsymbol{Q}^T & \boldsymbol{C} + \boldsymbol{H} + \boldsymbol{H}_{d,p} & \boldsymbol{H}_{d,d} \\ \boldsymbol{Q}_d^T + \boldsymbol{H}_{dp,u} & \boldsymbol{H}_{d,d}^T & \boldsymbol{H}_{d,dp} + \boldsymbol{H}_{dp,dp} \end{bmatrix} \begin{bmatrix} \mathrm{d}\boldsymbol{u} \\ \mathrm{d}\boldsymbol{p} \\ \mathrm{d}\boldsymbol{p}_d \end{bmatrix} = \begin{bmatrix} \boldsymbol{f}_{ext} \\ \boldsymbol{q}_{ext} \\ \boldsymbol{q}_{d,ext} \end{bmatrix} - \begin{bmatrix} \boldsymbol{f}_{int} + \boldsymbol{f}_d \\ \boldsymbol{q}_{int} + \boldsymbol{q}_d \\ \boldsymbol{q}_{d,int} + \boldsymbol{q}_{d,d} \end{bmatrix} \tag{52}$$

The tangent stiffness submatrices are given in Appendix A. It is noted that the history variable used for the cohesive zone model is updated after each converged time step. The fracture propagation criterion is also checked after each converged time step. This results in the fracture only propagating based on an equilibrium state.

We have verified the implementation of the non-Newtonian fluid flow inside the bulk by a comparison with the MATLAB partial differential equation solver. Results obtained for Newtonian fluids, including flow inside the fracture, have been compared with an example of a curved beam [14] and were also in good agreement. Unfortunately, due to the absence of analytical solutions for non-Newtonian fluids in fractured poro-elastic media, no verification was possible of the implementation of the non-Newtonian flow terms in the fracture.

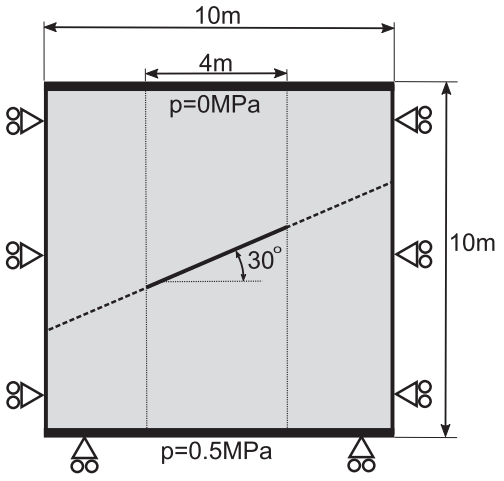

Fig. 4. Geometry and boundary conditions of the example used to illustrate the effects of lumped integration.

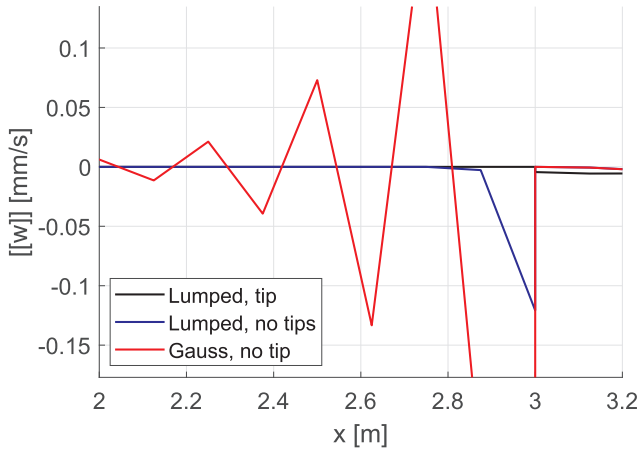

Fig. 6. Difference between fracture inflow and outflow ($w^+ - w^-$) with and without lumped integration and special treatment of the fracture tips. Results are shown for the left fracture tip.

4. The effect of lumped integration

To illustrate the effect of the fracture tip integration scheme described in Fig. 3 and the effect of using lumped integration compared to a Gauss integration scheme, a typical boundary value problem has been simulated [14]. This problem, shown in Fig. 4, consists of a square plate of 10 × 10 m with the centre 4 m fractured under a 30° angle. The left and right edges are constrained in the horizontal direction, while the bottom is constrained in the vertical direction. A pressure difference of 0.5 MPa is applied between the top and bottom edges.

The simulations have been carried out using the following properties of the solid: Young's modulus $E = 9$ GPa, Poisson ratio $\nu = 0.4$, Biot modulus $M = 1{\cdot}10^{18}$ MPa, Biot coefficient $\alpha = 1.0$, porosity $n_f = 0.3$, intrinsic permeability $k = 1{\cdot}10^{-12}$ m^2 and an interface permeability of $k_i = 1{\cdot}10^{-10}$ m/Pa s. The properties of the fluid were: Fluid index $n = 1.0$ (a Newtonian fluid) and base viscosity $\mu_0 = 1.0$ mPa s.

The domain was discretised using 80 × 40 Bézier extracted elements. A time-step size $\Delta t = 1$ s has been used. The simulations reached a steady state at $t = 40$ s. A dummy permeability for the unfractured elements of $k_{i,d} = 0.5{\cdot}10^{-3}$ m/Pa s and a dummy stiffness $d_n = d_s = 10^3$ GPa have been used.

The fluid velocity normal to the discontinuity is shown in Fig. 5. Large oscillations arise when a Gauss integration scheme is used. In contrast, when using a lumped integration scheme these oscillations do not occur. Looking at the difference between the top and bottom

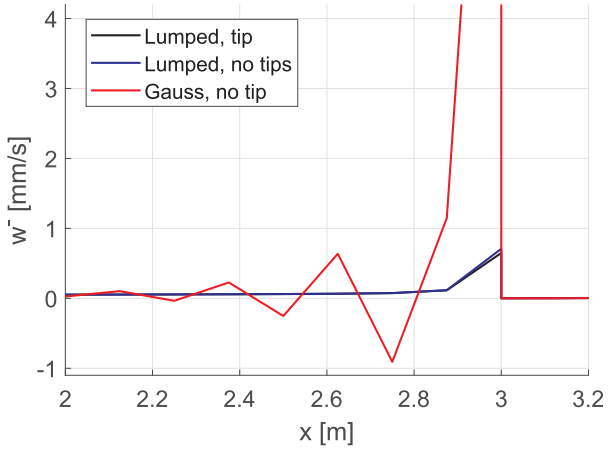

Fig. 5. Fluid velocity through the bottom interface (Γ^-) of the discontinuity (w^-) with and without lumped integration and special treatment of the fracture tips. Results are shown for the left fracture tip.

velocities through the interface, Fig. 6, similar oscillations are observed. This indicates that the oscillations at Γ^+ and Γ^- do not cancel each other. The result is small amounts of fluid being absorbed and released at different locations for the non-fractured interface elements when a Gauss integration scheme is used.

The result using lumped integration without the tip integration shows a large peak in the fracture inflow, Fig. 6, which does not occur when using the fracture tip integration. A large (positive) peak also occurs near the right fracture tip (not shown). This indicates that large amounts of fluid enter at the left tip, and leave the fracture at the right tip. This is confirmed by the pressure inside the discontinuity shown in Fig. 7. The slope of the pressure without tip integration pressure is steep compared to that with tip integration. This indicates that more fluid is being transported inside the fracture when no tip integration is used.

We therefore conclude that crack tip integration is necessary to prevent a non-physical inflow at the fracture tips. It is noted that this inflow problem at the tip is solely caused since the interface elements have also been inserted at places where fracture does not occur, or has not yet occurred. When interface elements are placed only where fracture has actually occurred, for instance adaptively using remeshing for propagating cracks, no dummy permeability is needed. This removes the coupling between the interior of the fracture and the interstitial fluid pressure using the dummy permeability, and therefore removes the non-physical fluid leak-off from the fracture tips and the need for the special fracture tip integration.

5. Case study of hydraulic fracturing

To analyse the influence of non-Newtonian fluids on the fracture propagation speed, a typical hydraulic fracturing problem has been simulated. The problem consists of a square plate of 0.25 m× 0.25 m, with a horizontal discontinuity through the centre of the plate, shown in Fig. 8. The first 5 mm of the discontinuity are pre-fractured, and an inflow of $Q_{tip} = 1{\cdot}10^{-5}$ m^2/ s is imposed on the left end of this fracture. The top, bottom and right edges are fully constrained in the horizontal and vertical directions, and a constant pressure of 0 MPa is imposed on these edges. The left edge is constrained horizontally, and no flow is allowed through this edge.

The simulations have been carried out using the following material properties: Young's modulus $E = 25.85$ GPa, Poisson ratio $\nu = 0.18$, bulk modulus $K_s = 13.46$ GPa, Biot coefficient $\alpha = 1.0$, tensile strength of the material $f_t = 1.7$ MPa, and a mode-I fracture toughness $G_{Ic} = 0.1$ kN/m. The bulk modulus of the fluid has been taken as $K_f = 0.2$ GPa and the porosity as $n_f = 0.2$.

The non-Newtonian fluids have been simulated with a constant base

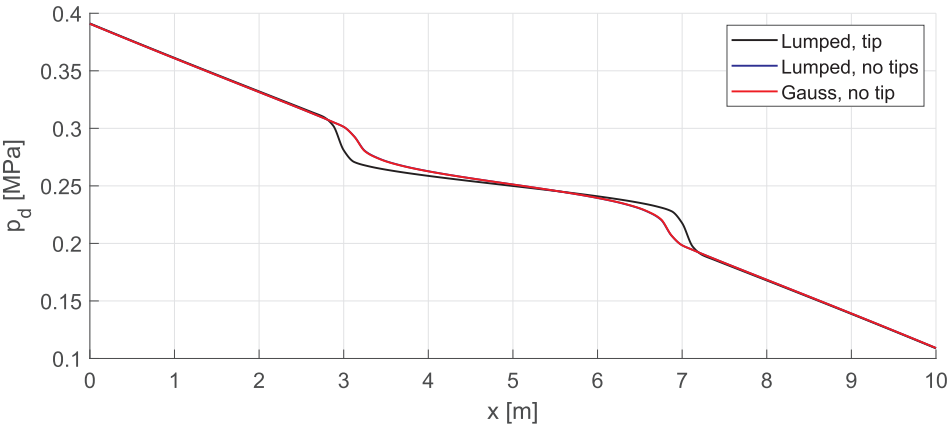

Fig. 7. Pressure inside the discontinuity, p_d, with and without lumped integration and special treatment of the fracture tips. The lumped integration without fracture tip integration matches the Gauss integration scheme.

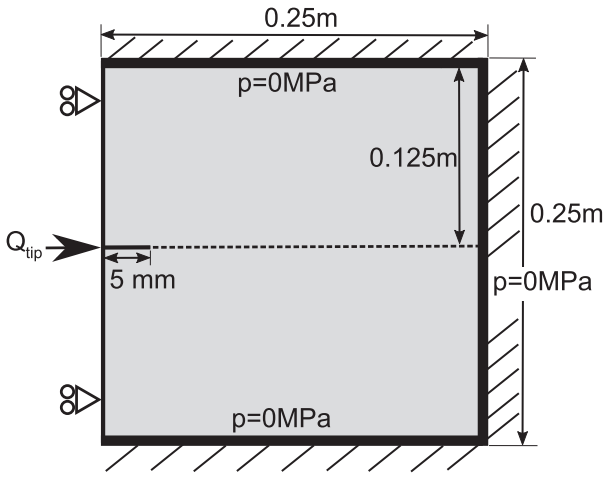

Fig. 8. Geometry and boundary conditions used for the hydraulic fracturing example.

viscosity $\mu_0 = 0.5$ mPa s^n, and five different power-law fluid indices have been adopted: Shear-thinning fluids with $n = 0.8$ and $n = 0.9$, a Newtonian fluid with $n = 1.0$, and shear-thickening fluids with $n = 1.1$ and $n = 1.2$. The amount of fluid leaking from the fracture into the surrounding porous medium has been varied by using three different permeabilities: $k = 1{\cdot}10^{-16}$ m^2, $k = 1{\cdot}10^{-17}$ m^2 and $k = 1{\cdot}10^{-18}$ m^2. The interface permeability has been assumed as $k_i = 1{\cdot}10^{-10}$ m/Pa s, and the interface permeability of the cohesive zone has been assumed to be equal to that of a fully open crack. The amount of fluid leaking from the fracture was influenced by varying the permeability of the porous medium, rather than the interface permeability, since the dependence of the effective permeability k_f^* on the fluid index and viscosity were known, whereas no relation was available for the dependence of the interface permeability on these properties.

The simulations have been carried out using a dummy interface permeability $k_{i,d} = 1{\cdot}10^{-3}$ m/Pa s and dummy stiffnesses $d_s = d_n = 5{\cdot}10^3$ GPa. The domain has been discretised using 250×20 Bézier extracted elements. The horizontal element size was constant at $dx = 1$ mm, while the vertical elements were taken smaller near the fracture, ranging from $dy = 3$ mm close to the discontinuity till $dy = 55$ mm for the elements near the top and bottom. A constant time-step size of $\Delta t = 1$ ms has been used, for the total simulation time of 0.5 s.

The fluid pressure inside the porous medium is shown in Fig. 9, where a low and a high value of the permeability have been considered. Clearly, the differences in pressure contours are much bigger for the shear-thinning fluids, with also more fluid flowing from the fracture to the surrounding porous medium. Further, a clear difference is observed between the cases of low and high values of the permeability, and is more pronounced for the shear-thinning fluid.

The fracture length for a permeability $k = 1{\cdot}10^{-16}$ m^2 is given in Fig. 10a. The results show that the larger leak-off for shear-thinning fluids significantly decreases the propagation length compared to the Newtonian fluid. Conversely, the smaller leak-off for shear-thickening

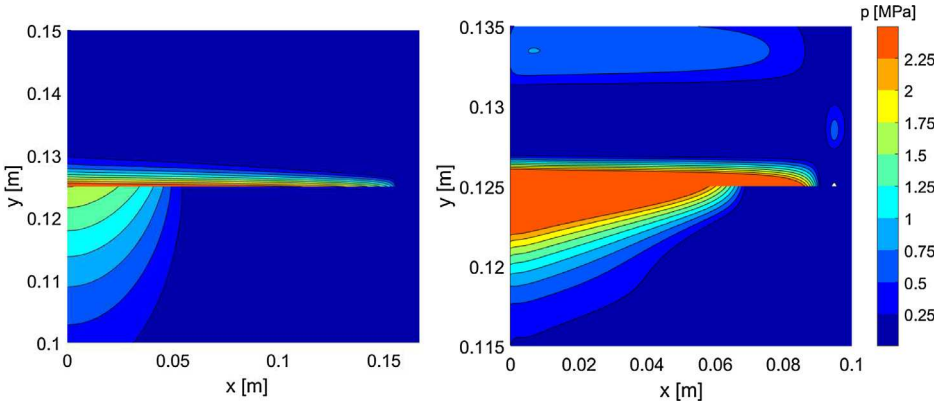

(a) Shear-thinning $n = 0.8$ (b) Shear-thickening $n = 1.2$

Fig. 9. Fluid pressure inside the porous medium for $k = 1{\cdot}10^{-16}$ m^2 (displayed in the lower part of each figure) and $k = 1{\cdot}10^{-18}$ m^2 (displayed in the upper part of each figure) at $t = 0.25$ s.

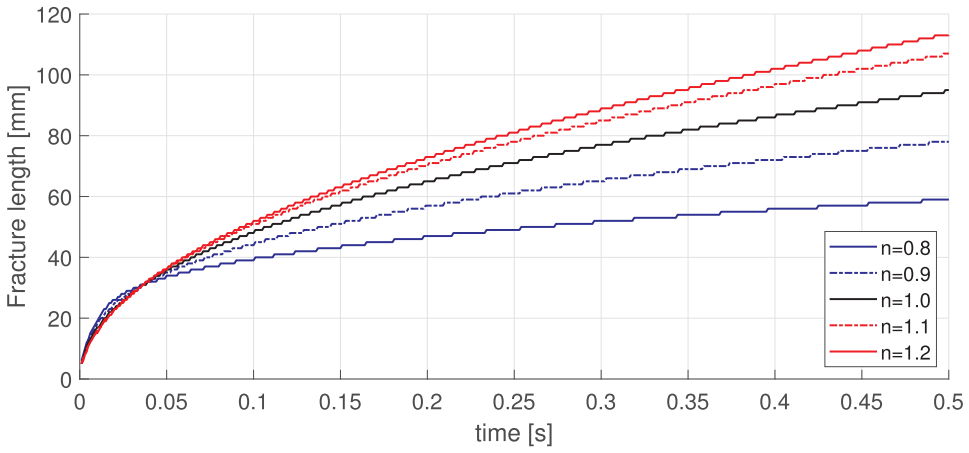

(a) $k = 1 \cdot 10^{-16}\mathrm{m}^2$

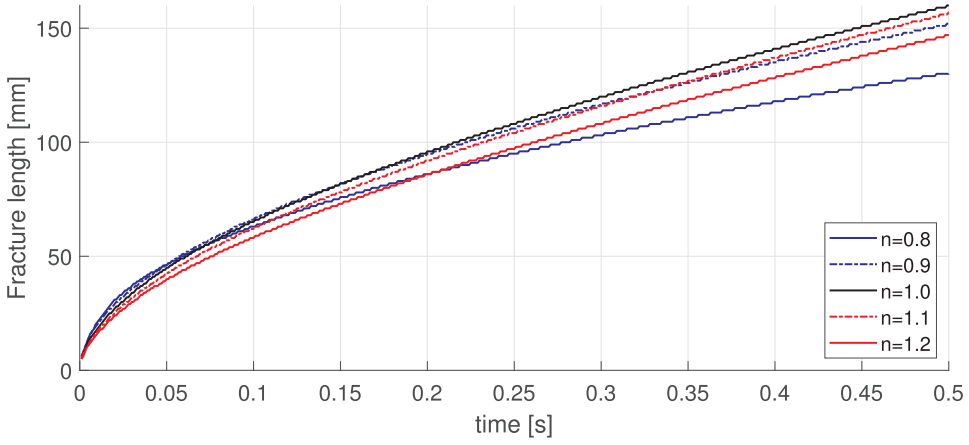

(b) $k = 1 \cdot 10^{-17}\mathrm{m}^2$

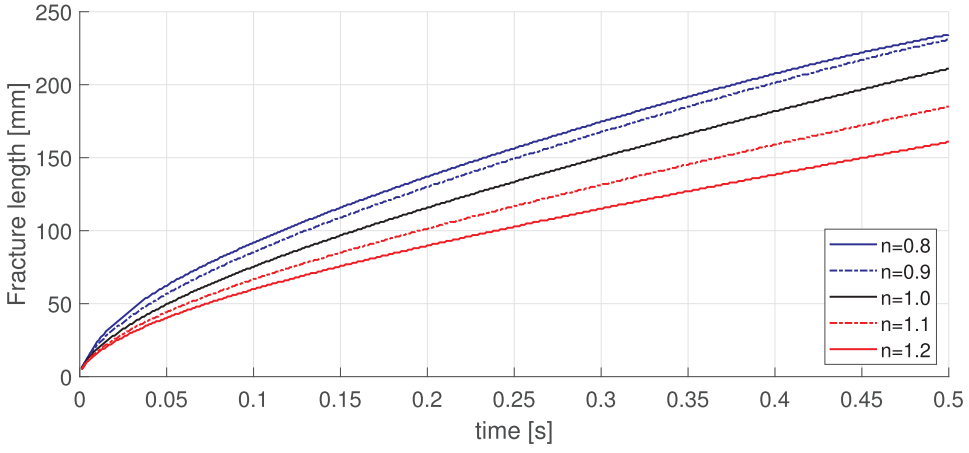

(c) $k = 1 \cdot 10^{-18}\mathrm{m}^2$

Fig. 10. Fracture length.

fluids results in a faster fracture propagation. This also comes out in Fig. 11c, which shows large differences in the fracture outflow velocity between Newtonian, shear-thinning and shear-thickening fluids. The lower amount of fluid flowing from the fracture to the porous medium for shear-thickening fluids results in higher pressures inside the fracture, as shown in Fig. 11b. But while the pressure of the shear-thickening fluid is much higher near the inlet, this pressure becomes negative near the fracture tip. This negative pressure is a result of the shear-thickening fluid having a high effective viscosity due to the small fracture opening height, and therefore flowing rather slowly towards the fracture tip. Since the effective viscosity of shear-thinning fluids is much lower than the shear-thickening fluids, this negative pressure near the fracture tip does not occur. Finally, the higher pressure inside the fracture for shear-thickening fluids results in a larger fracture opening, see Fig. 11a.

The fracture propagation for $k = 1{\cdot}10^{-18}\,\mathrm{m}^2$, Fig. 10c, shows the opposite behaviour from that observed before, with the fracture propagating faster for shear-thinning fluids. The difference in fracture length between $n = 0.8$ and $n = 0.9$ is rather small, whereas the fracture length difference between $n = 1.1$ and $n = 1.2$ is much larger. Looking

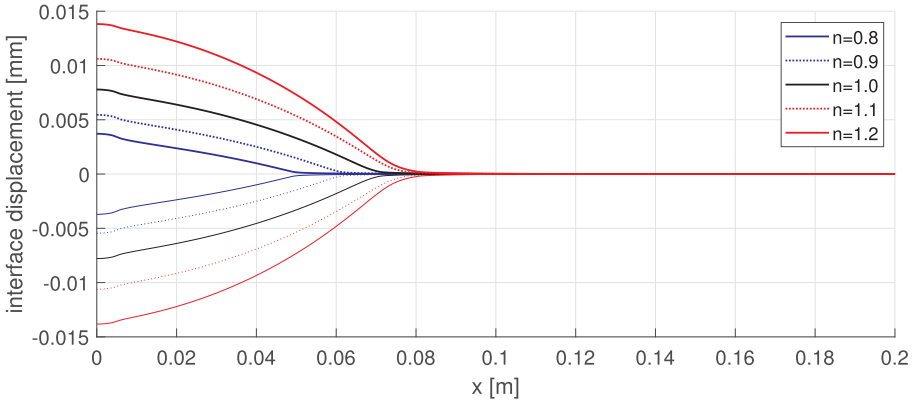

(a) Displacement at the interface, equal to half the fracture opening height, $\frac{1}{2}h$

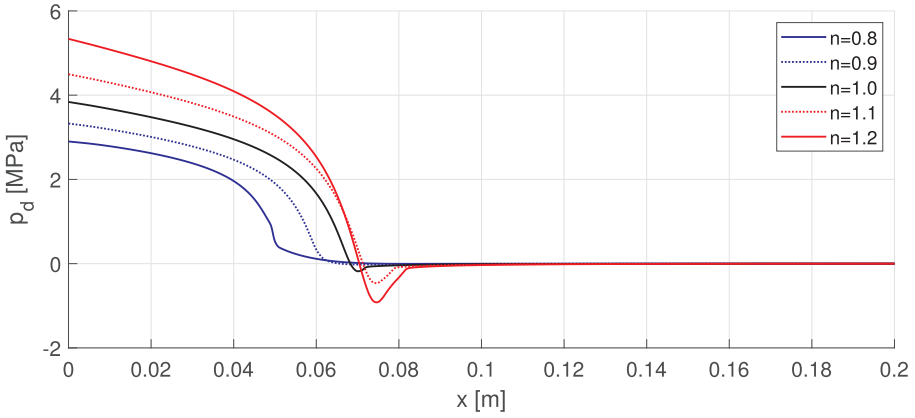

(b) Pressure inside the discontinuity, p_d

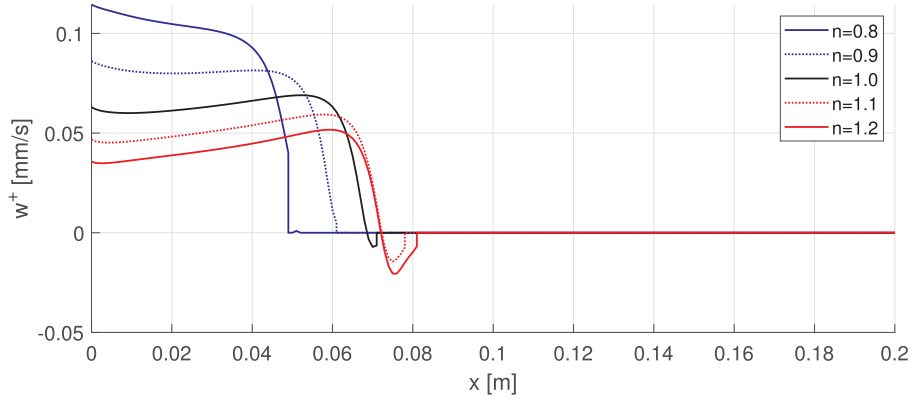

(c) Fracture outflow velocity, w^+

Fig. 11. Results for $k = 1{\cdot}10^{-16}$ m^2 at $t = 0.25$ s along the first 0.2 m of the discontinuity.

at the pressure inside the fracture, Fig. 13b, large differences can be observed. Whereas the fracture opening results in a locally negative pressure for shear-thickening fluids, no such negative pressure occurs for the shear-thinning fluids. This pressure is more negative than for the $k = 1{\cdot}10^{-16}$ m^2 case, explaining the slower fracture propagation compared to that for the Newtonian fluid. This negative pressure also causes fluid to flow from the porous medium into the fracture near the fracture tip, Fig. 13c. Somewhat further away from the fracture tip large outflows occur. These outflows are caused by the low diffusion inside the porous medium, resulting in large pressure differences between the recently pressurised fracture and the interstitial fluid. These outflows are further increased by the fracture having absorbed fluid from the porous medium at the fracture tip in the case of shear-thickening fluids. The outflow is also significantly higher for $n = 0.8$, compared to $n = 0.9$. This explains the limited difference in fracture propagation length between these two cases: Even though the pressure near the fracture tip is slightly higher, the effect on the propagation speed is mostly offset by the increased leak-off, resulting in a lower pressure inside the fracture.

The effects of a decreased fracture propagation due to leak-off for shear-thinning fluids, and negative fracture tip pressures for shear-thickening fluids are also seen in the results for $k = 1{\cdot}10^{-17}$ m^2. In this case, for the shear-thinning and for the shear-thickening fluids propagation is slower than for the Newtonian fluid, see Fig. 10b. The pressure at the crack tip in Fig. 12b is indeed negative for shear-thickening fluids, and positive for shear-thinning fluids. Furthermore, the shear-thinning fluids have significantly more leak-off from the fracture, as seen in Fig. 12c. It is observed that for the shear-thinning fluids

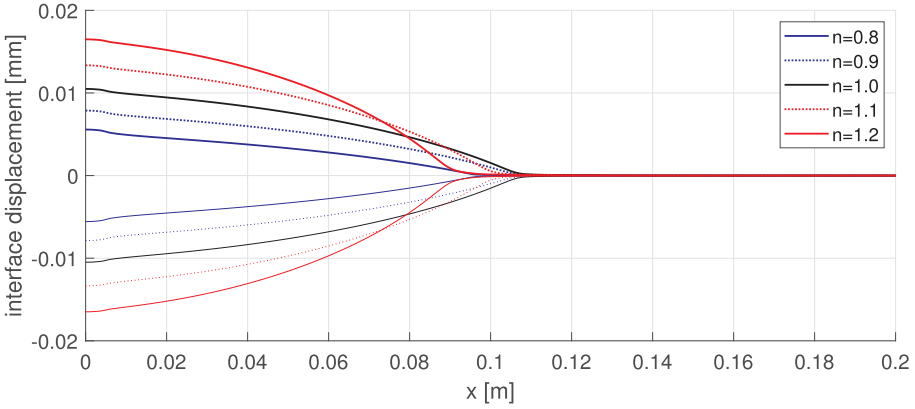

(a) Displacement at the interface, equal to half the fracture opening height, $\frac{1}{2}h$

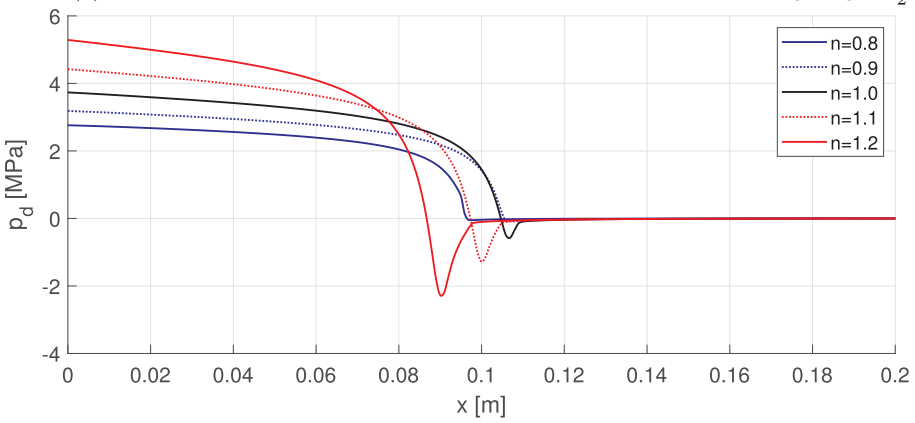

(b) Pressure inside the discontinuity, p_d

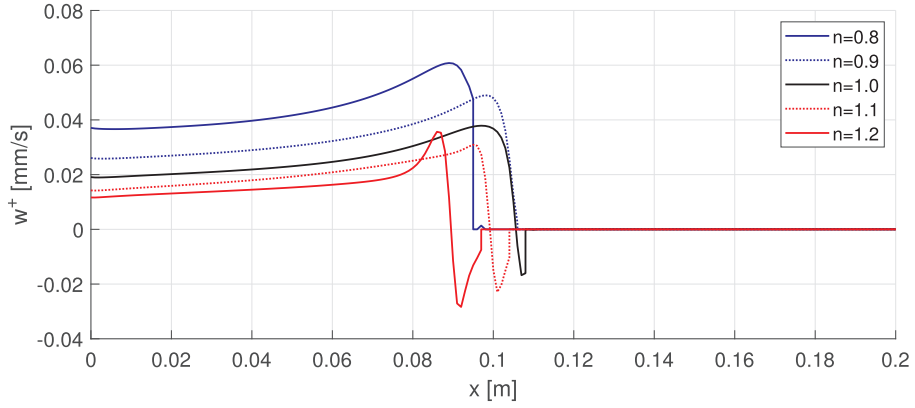

(c) Fracture outflow velocity, w^+

Fig. 12. Results for $k = 1{\cdot}10^{-17}$ m^2 at $t = 0.25$ s along the first 0.2 m of the discontinuity.

propagation is faster than for a Newtonian fluid and only slows down when the fracture has propagated further. This is because leak-off becomes more important for longer fractures.

It is finally noted that Fig. 10 shows some stepwise fracture propagation. This is caused by the finite mesh size (250 elements in the horizontal direction) in combination with the fact that the fracture is allowed to propagate only on a per-element basis. The stepwise propagation of Fig. 10 therefore does not have a direct physical basis. Nevertheless, stepwise fracture propagation of internally pressurised cracks has been observed experimentally [32]. Numerical models have been shown capable of capturing this effect, for instance when the solid is modelled using a lattice [33].

6. Concluding remarks

We have presented a model to simulate non-Newtonian (power-law) fluid flows inside pressurised fractures and deformable porous media. The discretisation has been done using Non-Uniform Rational B-Splines (NURBS), which have been cast in a standard finite element format using Bézier extraction. A major advantage of this isogeometric analysis approach is that the stresses, and the fluid pressures and velocities remain continuous at element boundaries, inside the porous medium as well as within the fracture. The fracture has been discretised using isogeometric interface elements, and an independent pressure degree of freedom was added into these elements to allow for the simulation of internally pressurised fractures.

It has been shown that the use of a lumped integration scheme is

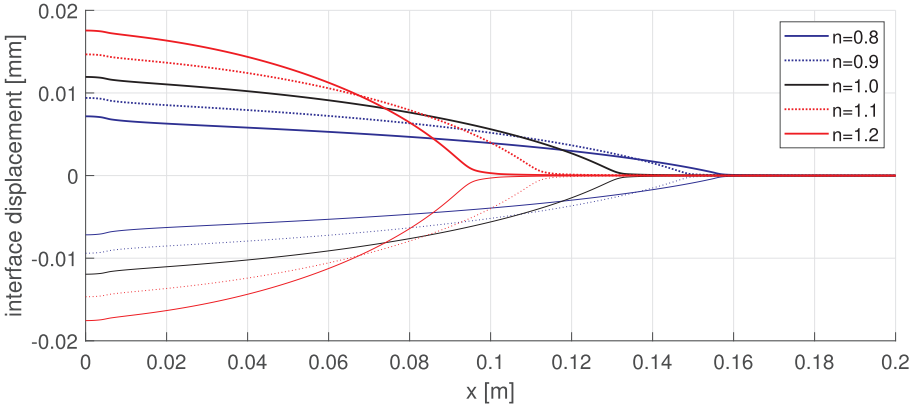

(a) Displacement at the interface, equal to half the fracture opening height, $\frac{1}{2}h$

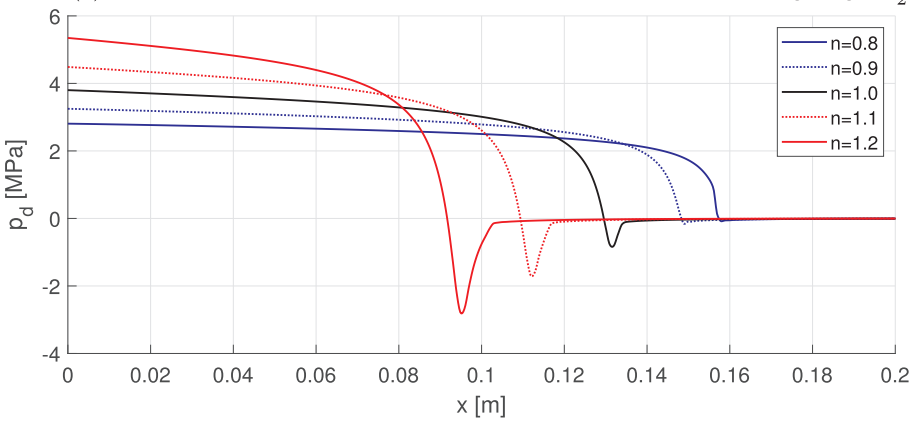

(b) Pressure inside the discontinuity, p_d

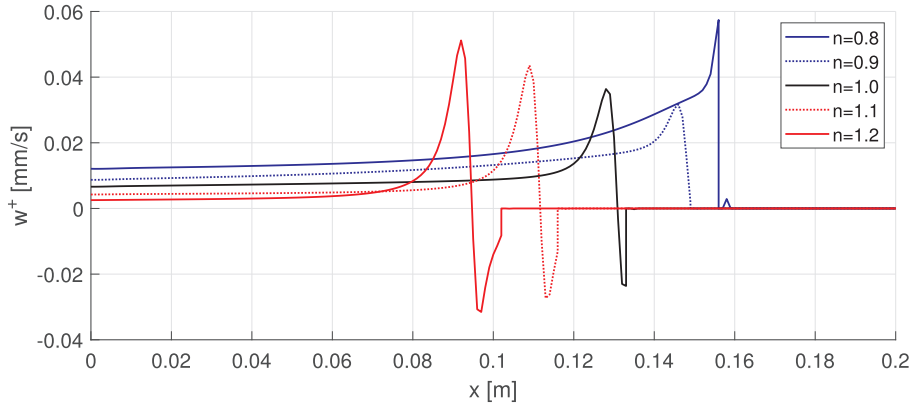

(c) Fracture outflow velocity, w^+

Fig. 13. Results for $k = 1{\cdot}10^{-18}$ m^2 at $t = 0.25$ s along the first 0.2 m of the discontinuity.

necessary, not only to prevent traction oscillations in interface elements that have not yet fractured, but also to obtain oscillation-free velocity profiles for the fracture inflow. At the fracture tips, a special integration scheme was applied to avoid high amounts of non-physical fluid leak-off. Results with and without this scheme have shown its importance in avoiding non-physical local fluid leak-off, and for the pressure inside the fracture.

Simulations have been carried out using different values of the index of a power-law fluid and the permeability of the surrounding porous medium. The simulations show differences in fracture propagation speed between the Newtonian and non-Newtonian fluids. Shear-thinning fluids yielded more fluid leak-off, while resulting in higher pressures near the fracture tip compared to Newtonian fluids. In contrast, shear-thickening fluids showed less fluid leak-off from the fracture, but their higher effective viscosity inside the fracture resulted in negative pressures close to the fracture tip.

The result is that shear-thinning fluids give rise to a faster fracture propagation in case of low permeabilities of the surrounding porous medium. On the other hand, shear-thickening fluids yield faster crack propagation when the permeability in the surrounding porous medium is high. Conversely, both shear-thickening and shear-thinning fluids can experience a slower fracture propagation compared to Newtonian fluids, depending on the porosity of the surrounding medium.

Acknowledgement

Financial support through H2020 European Research Council Advanced Grant 664734 “PoroFrac” is gratefully acknowledged.

Appendix A. Tangential stiffness matrices

The tangential stiffness submatrices used in Eq. (52) reads as follows:

$$\boldsymbol{K} = \frac{\partial \boldsymbol{f}_{int}}{\partial \boldsymbol{u}} = \int_{\Omega} \boldsymbol{B}^T \boldsymbol{D} \boldsymbol{B} \, \mathrm{d}\Omega \tag{A.1}$$

$$\boldsymbol{K}_d = \frac{\partial \boldsymbol{f}_d}{\partial \boldsymbol{u}} = \int_{\Gamma_d} \boldsymbol{N}_{ds}^T \boldsymbol{R}^T \boldsymbol{D}_d \boldsymbol{R} \boldsymbol{N}_{ds} \, \mathrm{d}\Gamma \tag{A.2}$$

$$\boldsymbol{Q} = \frac{\partial \boldsymbol{f}_{int}}{\partial \boldsymbol{p}} = -\int_{\Omega} \alpha \boldsymbol{B}^T \boldsymbol{m} \boldsymbol{N}_f \, \mathrm{d}\Omega \tag{A.3}$$

$$\boldsymbol{Q}_d = \frac{\partial \boldsymbol{f}_d}{\partial \boldsymbol{p}_d} = -\int_{\Gamma_d} \boldsymbol{N}_{ds}^T \boldsymbol{n}_{\Gamma_d} \boldsymbol{N}_d \mathrm{d}\Gamma \tag{A.4}$$

$$\boldsymbol{C} = \frac{\partial \boldsymbol{q}_{int1}}{\partial \boldsymbol{p}} = -\int_{\Omega} \frac{1}{M} \boldsymbol{N}_f^T \boldsymbol{N}_f \, \mathrm{d}\Omega \tag{A.5}$$

$$\boldsymbol{H} = \frac{\partial \boldsymbol{q}_{int2}}{\partial \boldsymbol{p}} = -\int_{\Omega} \frac{k_f^* \Delta t}{n} \, |\nabla \boldsymbol{p}^{t+\Delta t}|^{\frac{1}{n}-1} (\nabla \boldsymbol{N}_f)^T \nabla \boldsymbol{N}_f \, \mathrm{d}\Omega \tag{A.6}$$

$$\boldsymbol{H}_{d,p} = \frac{\partial \boldsymbol{q}_d}{\partial \boldsymbol{p}} = -\int_{\Gamma_d^{\pm}} k_i^{el} \Delta t \boldsymbol{N}_f^T \boldsymbol{N}_f \, \mathrm{d}\Gamma \tag{A.7}$$

$$\boldsymbol{H}_{d,d} = \frac{\partial \boldsymbol{q}_d}{\partial \boldsymbol{p}_d} = \int_{\Gamma_d^{\pm}} k_i^{el} \Delta t \boldsymbol{N}_f^T \boldsymbol{N}_d \, \mathrm{d}\Gamma \tag{A.8}$$

$$\boldsymbol{H}_{d,dp} = \frac{\partial \boldsymbol{q}_{d,d}}{\partial \boldsymbol{p}_d} = -2\int_{\Gamma_d} k_i^{el} \Delta t \boldsymbol{N}_d^T \boldsymbol{N}_d \, \mathrm{d}\Gamma \tag{A.9}$$

$$\boldsymbol{H}_{dp,u} = \frac{\partial \boldsymbol{q}_{d,int}}{\partial \boldsymbol{u}} = -\int_{\Gamma_d} \Delta t \mu_0^{-\frac{1}{n}} \, |\nabla \boldsymbol{N}_d \boldsymbol{p}_d^{t+\Delta t}|^{\frac{1}{n}-1} \left(\frac{\boldsymbol{n}_{\Gamma_d} \boldsymbol{N}_{ds} \boldsymbol{u}^{t+\Delta t}}{2} \right)^{\frac{1}{n}+1} \nabla \boldsymbol{N}_d \boldsymbol{p}_d^{t+\Delta t} \nabla \, \boldsymbol{N}_d^T \boldsymbol{n}_{\Gamma_d} \boldsymbol{N}_{ds} \, \mathrm{d}\Gamma \tag{A.10}$$

$$\boldsymbol{H}_{dp,dp} = \frac{\partial \boldsymbol{q}_{d,int}}{\partial \boldsymbol{p}_d} = -\int_{\Gamma_d} \Delta t \frac{2}{2n+1} \mu_0^{-\frac{1}{n}} \, |\nabla \boldsymbol{N}_d \boldsymbol{p}_d^{t+\Delta t}|^{\frac{1}{n}-1} \left(\frac{\boldsymbol{n}_{\Gamma_d} \boldsymbol{N}_{ds} \boldsymbol{u}^{t+\Delta t}}{2} \right)^{\frac{1}{n}+2} \nabla \, \boldsymbol{N}_d^T \nabla \boldsymbol{N}_d \, \mathrm{d}\Gamma \tag{A.11}$$

References

[1] Boone TJ, Ingraffea AR. A numerical procedure for simulation of hydraulically-driven fracture propagation in poroelastic media. Int J Numer Anal Meth Geomech 1990;14:27–47.
[2] Segura JM, Carol I. Coupled HM analysis using zero-thickness interface elements with double nodes. Part I: theoretical model. Int J Numer Anal Meth Geomech 2008;32:2083–101.
[3] Simoni L, Secchi S. Cohesive fracture mechanics for a multi-phase porous medium. Eng Comput 2003;20:675–98.
[4] Secchi S, Simoni L, Schrefler BA. Mesh adaptation and transfer schemes for discrete fracture propagation in porous materials. Int J Numer Anal Meth Geomech 2007;31:331–45.
[5] de Borst R, Réthoré J, Abellan M-A. A numerical approach for arbitrary cracks in a fluid-saturated medium. Arch Appl Mech 2006;75(10–12):595–606.
[6] Réthoré J, de Borst R, Abellan M-A. A two-scale approach for fluid flow in fractured porous media. Int J Numer Meth Eng 2007;71:780–800.
[7] Mohammadnejad T, Khoei AR. Hydro-mechanical modeling of cohesive crack propagation in multiphase porous media using the extended finite element method. Int J Numer Anal Meth Geomech 2013;37:1247–79.
[8] Remij EW, Remmers JJC, Huyghe JM, Smeulders DMJ. The enhanced local pressure model for the accurate analysis of fluid pressure driven fracture in porous materials. Comput Methods Appl Mech Eng 2015;286:293–312.
[9] Zhao J, Jiang Y, Li Y, Zhou X, Wang R. Modeling fractures and barriers as interfaces for porous flow with extended finite-element method. J Hydrol Eng 2018;23:04018024.
[10] Miehe C, Mauthe S. Phase field modeling of fracture in multi-physics problems. Part III. Crack driving forces in hydro-poro-elasticity and hydraulic fracturing of fluid-saturated porous media. Comput Methods Appl Mech Eng 2016;304:619–55.
[11] Borden MJ, Scott MA, Evans JA, Hughes TJR. Isogeometric finite element data structures based on Bézier extraction of NURBS. Int J Numer Meth Eng 2011;87:15–47.
[12] Vignollet J, May S, de Borst R. On the numerical integration of isogeometric interface elements. Int J Numer Meth Eng 2015;102:1733–49.
[13] Irzal F, Remmers JJC, Verhoosel CV, de Borst R. An isogeometric analysis Bézier interface element for mechanical and poromechanical fracture problems. Int J Numer Meth Eng 2014;97:608–28.
[14] Vignollet J, May S, de Borst R. Isogeometric analysis of fluid-saturated porous media including flow in the cracks. Int J Numer Meth Eng 2016;108:990–1006.
[15] Carrier B, Granet S. Numerical modeling of hydraulic fracture problem in permeable medium using cohesive zone model. Eng Fract Mech 2012;79:312–28.
[16] de Borst R. Computational methods for fracture in porous media. Elsevier; 2017.
[17] de Borst R. Fluid flow in fractured and fracturing porous media: a unified view. Mech Res Commun 2017;80:47–57.
[18] Nguyen VP, Lian H, Rabczuk T, Bordas S. Modelling hydraulic fractures in porous media using flow cohesive interface elements. Eng Geol 2017;225:68–82.
[19] Zielonka MG, Searles KH, Ning J, Buechler SR. Development and validation of fully-coupled hydraulic fracturing simulation capabilities. Proceedings of the SIMULIA community conference, SCC2014. 2014. p. 19–21.
[20] Di Federico V, Pinelli M, Ugarelli R. Estimates of effective permeability for non-Newtonian fluid flow in randomly heterogeneous porous media. Stoch Env Res Risk Assess 2010;24:1067–76.
[21] Morais AF, Seybold H, Herrmann HJ, Andrade JS. Non-Newtonian fluid flow through three-dimensional disordered porous media. Phys Rev Lett 2009;103:194502.
[22] Bao K, Lavrov A, Nilsen HM. Numerical modeling of non-Newtonian fluid flow in fractures and porous media. Comput Geosci 2017;21:1313–24.
[23] Lavrov A. Numerical modeling of steady-state flow of a non-Newtonian power-law fluid in a rough-walled fracture. Comput Geotech 2013;50:101–9.
[24] Lavrov A. Redirection and channelization of power-law fluid flow in a rough-walled fracture. Chem Eng Sci 2013;99:81–8.
[25] Tagirova VR. Hydraulic fracture crack propagation driven by a non-Newtonian fluid. Moscow Univ Mech Bull 2009;64:135–42.
[26] Mikhailov DN, Economides MJ, Nikolaevskiy VN. Fluid leakoff determines hydraulic fracture dimensions: approximate solution for non-Newtonian fracturing fluid. Int J Eng Sci 2011;49:809–22.
[27] Hageman T, de Borst R. Flow of non-Newtonian fluids in fractured porous media: Isogeometric vs standard finite element discretisation. Int J Numer Analyt Methods Geomech 2019. https://doi.org/10.1002/nag.2948. [submitted for publication].
[28] Christopher RH, Middleman S. Power-law flow through a packed tube. Industr Eng Chem Fundam 1965;4:422–6.
[29] Al-Fariss T, Pinder KL. Flow through porous media of a shear-thinning liquid with yield stress. Can J Chem Eng 1987;65:391–405.
[30] Chapelle D, Bathe KJ. The inf-sup test. Comput Struct 1993;47:537–45.
[31] Schellekens JCJ, de Borst R. On the numerical integration of interface elements. Int J Numer Meth Eng 1993;36:43–66.
[32] L'homme TPY. Initiation of hydraulic fractures in natural sandstones [Ph.D. thesis]. Delft University of Technology; 2005.
[33] Peruzzo C, Cao DT, Milanese E, Favia P, Pesavento F, Hussain F, et al. Dynamics of fracturing saturated porous media and self-organization of rupture. Eur J Mech A Solids 2019;74:471–84.